Geophysical Research Letters

RESEARCH LETTER
10.1029/2023GL103733

Key Points:

- Filtered electric fields from the Swarm satellites agree with SuperDARN
- Variable and high-magnitude Poynting flux structures are embedded in and between field-aligned currents
- Poynting flux from sub-quasi-static dynamics can comprise as much as half of the total

Correspondence to:

D. D. Billett,
daniel.billett@usask.ca

Citation:

Billett, D. D., McWilliams, K. A., Ponomarenko, P. V., Martin, C. J., Knudsen, D. J., & Vines, S. K. (2023). Multi-scale ionospheric Poynting fluxes using ground and space-based observations. *Geophysical Research Letters*, *50*, e2023GL103733. https://doi.org/10.1029/2023GL103733

Received 17 MAR 2023
Accepted 12 MAY 2023

Multi-Scale Ionospheric Poynting Fluxes Using Ground and Space-Based Observations

D. D. Billett[1], K. A. McWilliams[1], P. V. Ponomarenko[1], C. J. Martin[1], D. J. Knudsen[2], and S. K. Vines[3]

[1]Institute of Space and Atmospheric Studies, University of Saskatchewan, Saskatoon, SK, Canada, [2]Department of Physics and Astronomy, University of Calgary, Calgary, AB, Canada, [3]Johns Hopkins Applied Physics Laboratory, Laurel, MD, USA

Abstract Three events are presented where high-resolution measurements from the Swarm satellites coincided with excellent F-region ionospheric coverage from The Super Dual Auroral Radar Network (SuperDARN). Large-scale ionospheric convection patterns from SuperDARN, together with field-aligned-current patterns from he Active Magnetosphere and Planetary Response Experiment (AMPERE), provide information on quasi-static ionospheric dynamics traversed by Swarm. Because the Swarm observations and orbital path coincided with favorable SuperDARN/AMPERE observing conditions, it was possible to filter the Swarm electric field observations into a quasi-static component that agreed with the SuperDARN electric field. The residual electric field from Swarm is thus indicative of small- and mesoscale dynamics not captured by the convection and field-aligned current (FAC) patterns. Calculations of the Poynting flux between the different instruments show that dynamics on small-to mesoscales can be highly variable within structures like FACs. In the events shown, small- and medium-scale Poynting fluxes occasionally dominate over those from large-scale processes.

Plain Language Summary A significant amount of energy from the solar wind deposited into the upper atmosphere of Earth (above ∼100 km altitude) is contained within small-scale (on the order of kilometers) fluctuations of the electric field. This kind of variability is difficult to measure do the sparse resolution (both in space and time) of instruments like ground-based instruments, or the global fitting procedures of satellite constellations. Those instruments, which tend to focus on observing large-scale "big picture" dynamics, do however excel at providing important information about the global state of the upper atmosphere. Small-scale (∼1 km) data from the Swarm satellites is used in this letter, in conjunction with ground-based radars and a satellite constellation, to obtain a complete picture of how space weather energy dissipation is spread across all scale sizes. It is found that small features that only Swarm can see occasionally dominate in terms of energy balance.

1. Introduction

Electric and magnetic fields in the high-latitude ionosphere have been studied for decades as measures of magnetosphere-ionosphere-thermosphere coupling. At large scales, on the order of thousands of kilometers, Dungey cycle convection of the magnetosphere drives field-aligned currents (FACs) and ionospheric plasma convection (Cowley & Lockwood, 1992; Dungey, 1961; Iijima & Potemra, 1976; Weimer, 2001). These quasi-static or large-scale processes are typically well characterized by statistical datasets as being controlled by the orientation of the interplanetary magnetic field (e.g., Heppner & Maynard, 1987; Ruohoniemi & Greenwald, 1996), and encompass scale sizes on the order of thousands of kilometers. However, there are strong modes of spatial and temporal variability at small- and mesoscales tens and hundreds of kilometer scale sizes, respectively that are difficult to model (Cousins et al., 2013). Causes of sub-quasi-static variability are wide ranging (Yu et al., 2022), and include processes such as substorms (Grocott et al., 2009; Zou et al., 2009), particle precipitation (Billett et al., 2020; Senior et al., 2002), and sub-auroral polarisation streams (SAPS; Clausen et al., 2012; Billett, McWilliams, Kerr, et al., 2022). On the order of kilometeres, kinetic Alfveń waves drive a large degree of small-scale variability (Lühr et al., 2015).

Large-scale dynamics of the high-latitude ionosphere are notoriously difficult to decouple from small- and mesoscale dynamics. Ground-based instruments, such as incoherent and coherent scatter radars, magnetometers, and ionosondes, for example, excel at observing large-scale quasi-static structures due to consistently observing

a specific region of space. Satellites, on the other hand, can measure ionospheric electric and magnetic fields at a very high cadence in-situ, but cannot distinguish between spatial and temporal variations. It is often challenging to scrutinize high-resolution satellite measurements without fully being aware of the underlying quasi-static dynamics that are being traversed, such as large-scale Birkeland currents/FACs, convective flows, and auroral arcs. Whilst one might think that the quasi-static system is responsible for most of the electromagnetic energy being transferred between the magnetosphere and atmosphere (otherwise known as the Poynting flux), there is in fact a much more complicated and poorly understood balance of that energy across all spatial scales (Codrescu et al., 1995; Y. Deng & Ridley, 2007; Keiling et al., 2019). For example, recent work from Billett, McWilliams, Pakhotin, et al. (2022) estimated that the observed Poynting flux drops off rapidly when low-pass filtering high-resolution measurements from 1 to 15 km, and then drops off linearly to a ∼50% underestimation at around 1,000 km scale size (relative to 1 km scale sizes). Because no single instrument can fully capture the complex cross-scale dynamics that leads to this energy discrepancy, conjunctions between ground and space-based instrumentation are actively sought after, with the former often being referred to as providing a vital spatially extensive region of context for spacecraft observations without which the latter would be considerably less informative.

In this letter, multi-scale observations of the high-latitude ionosphere are presented using data from the Swarm satellite constellation, the Super Dual Auroral Radar Network (SuperDARN), and the Active Magnetosphere and Planetary Response Experiment (AMPERE). SuperDARN and AMPERE datasets provide global-scale maps of the ionospheric quasi-static electric and perturbation magnetic fields, respectively, whilst instruments on-board Swarm capture small and mesoscale variability. The residual variability in the Swarm data that is not captured by the large scale, quasi-static SuperDARN and AMPERE measurements is extracted. The quasi-static and residual Poynting fluxes are compared, revealing strong multi-scale structuring and variability embedded within the large-scale FACs.

2. Data

2.1. Swarm

The 16 Hz ion velocities and 50 Hz magnetic fields from Swarm A and B, at polar orbit altitudes of ∼460 km and ∼510 km, respectively, are obtained from the Thermal Ion Imager (TII; Knudsen et al., 2017) and Vector Field Magnetometer (VFM; Leger et al., 2009) instruments. VFM data is downsampled to 16 Hz (0.95 km scale size taking into account the Nyquist criterion, which states that the maximum resolvable frequency is half the sampling frequency) at the Swarm A orbit altitude by averaging for the purpose of this study, to remain consistent with the TII. "Spikey" noise in the ion drift data, defined as a single timestep where the velocity has a difference 300 m s^{-1} greater than both its neighbors, is corrected with the mean of its neighbors.

The Swarm electric field (**E**) is derived from the ion velocity (**v**) and magnetic field **B** through the relationship $\mathbf{E} = -\mathbf{v} \times \mathbf{B}$. A filtering scheme is then employed in order to separate the large-scale quasi-static system from the total electric field. A 225s Savitsky-Golay low-pass filter, as used in previous studies of Swarm derived Poynting flux (Billett, McWilliams, Pakhotin, et al., 2022; Ivarsen et al., 2020), produces this quasi-static electric field component ($\mathbf{E}_{\mathbf{static}}$, at a scale size of ∼3,400 km) and leaves a residual ($\delta\mathbf{E}$). After subtracting the terrestrial background field from the Swarm magnetic field using the International Geomagnetic Reference Field (IGRF; Alken et al., 2021) to get the perturbation ($\delta\mathbf{B}$), a quasi-static and residual Poynting flux is derived:

$$S_{\text{static}} = -\frac{1}{\mu_0}(\mathbf{E}_{\mathbf{static}} \times \delta\mathbf{B}) \cdot \hat{B} \tag{1}$$

$$S_{\text{residual}} = -\frac{1}{\mu_0}(\delta\mathbf{E} \times \delta\mathbf{B}) \cdot \hat{B} \tag{2}$$

where μ_0 is the permeability of free space and $\hat{B}$ is a unit vector in the magnetic field direction. Assuming variations in **E** and **B** are mostly horizontal, the Poynting fluxes derived from Equations 1 and 2 are completely in the magnetic field-aligned direction. Thus, the Swarm **E** and **B** data are additionally transformed into mean field-aligned coordinates (magnetic north, east, and field-algined) from satellite track orientated (along-track, cross-track, and vertical) prior to calculating the Poynting fluxes.

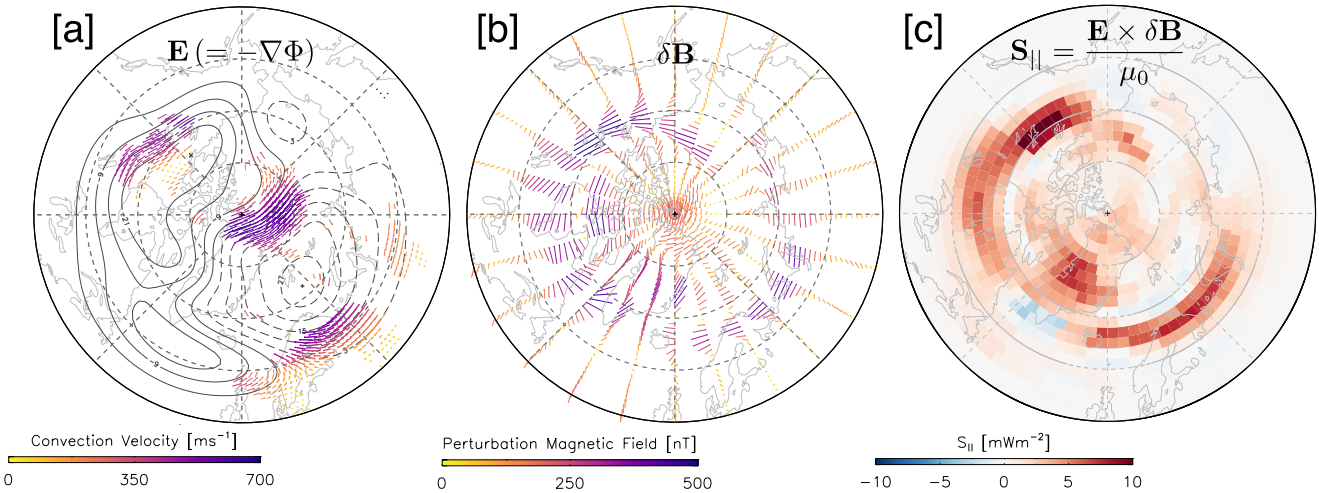

Figure 1. Example northern hemisphere Poynting flux calculation for 14 October 2013, 14:00 UT. (a) SuperDARN electric potential convection pattern with the locations of binned radar data colored as velocity vectors. (b) AMPERE perturbation magnetic fields. (c) Equivalent Poynting flux calculated on the same grid as AMPERE using (a, b). The coordinate system is Altitude Adjusted Corrected Geomagnetic (AACGM; Shepherd, 2014) latitude and local time, in a polar plot format with noon at the top and dawn to the right. The plot extends to 50° AACGM latitude in 10° segments.

2.2. SuperDARN and AMPERE

SuperDARN (Greenwald et al., 1995) consists of multiple high-frequency ground-based radars in both the northern and southern mid to high latitudes. Each radar measures the line-of-sight plasma velocity in the ionosphere by calculating the Doppler shift of high-frequency signals scattered by field-aligned electron density irregularities. At high-latitudes this plasma velocity mainly corresponds to the F-region convective ion-drift imposed on the ionosphere by the magnetospheric Dungey cycle, but could also be a result of mesoscale processes such as traveling ionospheric disturbances and magnetohydrodynamics waves. When line-of-sight velocity vectors from multiple SuperDARN radars are combined, a large-scale fit can be carried out to solve for the high-latitude electric potential (Φ) in a given hemisphere (Ruohoniemi & Baker, 1998). Utilizing the relationships $\mathbf{E} = -\nabla\Phi$ and $\mathbf{v} = (\mathbf{E}\times\mathbf{B})/B^2$, the contours of Φ relate directly to the ionospheric convection velocity and electric field. We utilize Northern hemisphere SuperDARN convection patterns are utilized in this letter, supplemented with an empirical model based on the statistical dependence of SuperDARN convection patterns to the interplanetary magnetic field (Thomas & Shepherd, 2018), to fill gaps in radar coverage. The integration time for a single convection map is nominally 2 min.

AMPERE (Anderson et al., 2014, 2021) provides global scale measurements of magnetic fields perturbed ($\delta\mathbf{B}$) due to FACs. These are obtained from the Iridium Communications Satellite Network constellation after subtracting the background terrestrial magnetic field from onboard magnetometer data using a main field reference model (IGRF or the World Magnetic Model (WMM; Chulliat et al., 2020), the former of which is used in this study), then fitting a spherical harmonic formulation (Waters et al., 2001, 2020). The $\delta\mathbf{B}$'s are related to the FAC densities, $\mathbf{J}$, by $\nabla\times\delta\mathbf{B} = \mu_0\mathbf{J}$. AMPERE fitted $\delta\mathbf{B}$'s and FAC's are produced at a 10 min integration and 2 min cadence. These fitted AMPERE data products are sampled onto a 1° magnetic latitude by 1 hr of magnetic local time (MLT) grid.

By using the global fits to $\mathbf{E}$ and $\delta\mathbf{B}$ from SuperDARN and AMPERE, the Poynting flux can be derived globally using Equation 1 (Billett, McWilliams, Perry, et al., 2022; Billett et al., 2021; Waters et al., 2004). Figure 1 shows an example SuperDARN/AMPERE Poynting flux calculation, illustrating that it is a powerful technique to achieve a data-driven snapshot of the global Poynting flux morphology. Given that both SuperDARN and AMPERE in this instance utilize fits which significantly smooth out spatiotemporal fluctuations in the ionospheric electric and magnetic fields, the resulting Poynting flux is treated as essentially quasi-static only.

It is additionally noted that because the Iridium satellites orbit at a high F-region altitude of ∼780 km, a correction for the curvature of the magnetic field is applied to the AMPERE $\delta\mathbf{B}$'s to project them to an altitude of 250 km (approximately the SuperDARN backscatter altitude, using the 3/2 relationship described by Knipp et al. (2014)). The same correction procedure is applied to the Swarm data.

2.3. Event Selection

The Swarm along-track ion velocities from the TII sensors contain significant errors (Lomidze et al., 2019) associated with variations in the satellite floating potential (Burchill & Knudsen, 2016). A strict selection criterion is therefore imposed for the events shown in this letter, to times where we expect the along-track ion-velocity to be small so that it can be set to zero. Because $\mathbf{E} = -\mathbf{v} \times \mathbf{B}$, the along-track ion-drift errors would propagate into the derived cross-track electric field. The SuperDARN plasma convection patterns are thus utilized, on an event-by-event basis, to find occurrences of when the Swarm orbital trajectory was parallel to the electric field (i.e., when along-track is aligned with the electric field) for extended periods of time. An example of when this scenario would happen is during a cross-polar-cap satellite pass which directly bisects a plasma convection cell, perpendicular to the ion-drift. The automated process employed to find such events involved finding where a Swarm satellite entered the polar cap (above 60° AACGM latitude) within 1 hr MLT of dawn/dusk, and then exited within 1 hr of dusk/dawn. This is of course not a perfect solution, because it is expected that SuperDARN convection patterns are poor at capturing variability much smaller than quasi-static scale sizes. However, it minimizes avoidable errors in the Swarm electric field for the purpose of comparisons with SuperDARN convection patterns. Previous studies have carried out comprehensive validations of the ion-drifts from Swarm, including comparisons with those from SuperDARN (Burchill & Knudsen, 2022; Fiori et al., 2016; Koustov et al., 2019; Lomidze et al., 2019).

Supplementary criteria for identifying good Swarm-SuperDARN-AMPERE conjunction events are more adaptable. Foremost is that there should be excellent SuperDARN data coverage in the region a Swarm satellite is flying over, using a preliminary binned vector threshold of 500 points for the whole map, to ensure the electric potential convection fit is well constrained (Walach et al., 2022). Second, both the SuperDARN convection and AMPERE FAC patterns should reasonably agree with each other, because it is expected that the convection and FAC boundary positions have a linear relationship (Clausen et al., 2013; Fogg et al., 2020). In practical terms, the high-latitude R1 FACs should approximately extend through the center of the convection cell, whilst the lower latitude R2 FACs should lie slightly poleward of the Hepnner-Maynard boundary. Discontinuity between a SuperDARN convection and AMPERE FAC pattern could be due to poor SuperDARN data coverage, or particularly harsh horizontal conductivity gradients (Sofko et al., 1995). However, the along-track electric field and SuperDARN data threshold criteria described above reduces the number of Swarm-SuperDARN-AMPERE northern hemisphere conjunction events significantly. Thus, the events were checked by hand for good convection/FAC agreement. From the total number of events, three northern hemisphere passes of Swarm A and B that matched the above criteria the best (e.g., because the convection and FAC patterns did not change much throughout the events) were chosen to show in this letter.

3. Results and Discussion

Figure 2 shows Swarm-SuperDARN-AMPERE comparisons during a polar pass from Swarm B on 18 February 2018. The data is segmented into 2-min intervals from which a new SuperDARN convection and AMPERE FAC pattern was generated, given at the top of each timeseries set. The black arrow shows the path of Swarm B during each segment as it bisects the plasma convection cells on the dawnside (panels a–e) and duskside (panels f–j). In panels (c) and (h) respectively, the satellite passes perpendicularly through the R1 and R2 FACs on the dawn and dusk sides. The timeseries, from top to bottom, show comparisons between northward electric fields, northward perturbation magnetic fields, eastward perturbation magnetic fields, and Poynting flux. The Kp index during this pass was low (2+).

The electric field comparisons in Figure 2 are between the SuperDARN convection (black), Swarm quasi-static (blue, $\mathbf{E}_{\mathbf{static}}$), and Swarm residual (red, $\delta\mathbf{E}$) components. Between (a) and (e), $\mathbf{E}_{\mathbf{static}}$ is negative (equatorward) until passing the center of the dawn convection cell, where it turns positive (northward) along with the SuperDARN electric field. As the direction of north and south changes as the spacecraft crosses the pole in panel (e), the sign of the SuperDARN electric field flips because the overall convection pattern orientation represents a dawn-to-dusk electric field. Swarm $\mathbf{E}_{\mathbf{static}}$ also flips sign and matches the SuperDARN trace almost identically in panel (f), but a rapid convection pattern change in (g) in the same region causes discontinuity. This change is due to a difference in the supplemented empirical convection model between panels (f) and (g), as it is categorized by discreet interplanetary magnetic field bins which were crossed at that time. It is also likely that the low coverage of SuperDARN radar data poleward of the dusk cell exacerbates the discontinuity between the convection fit and

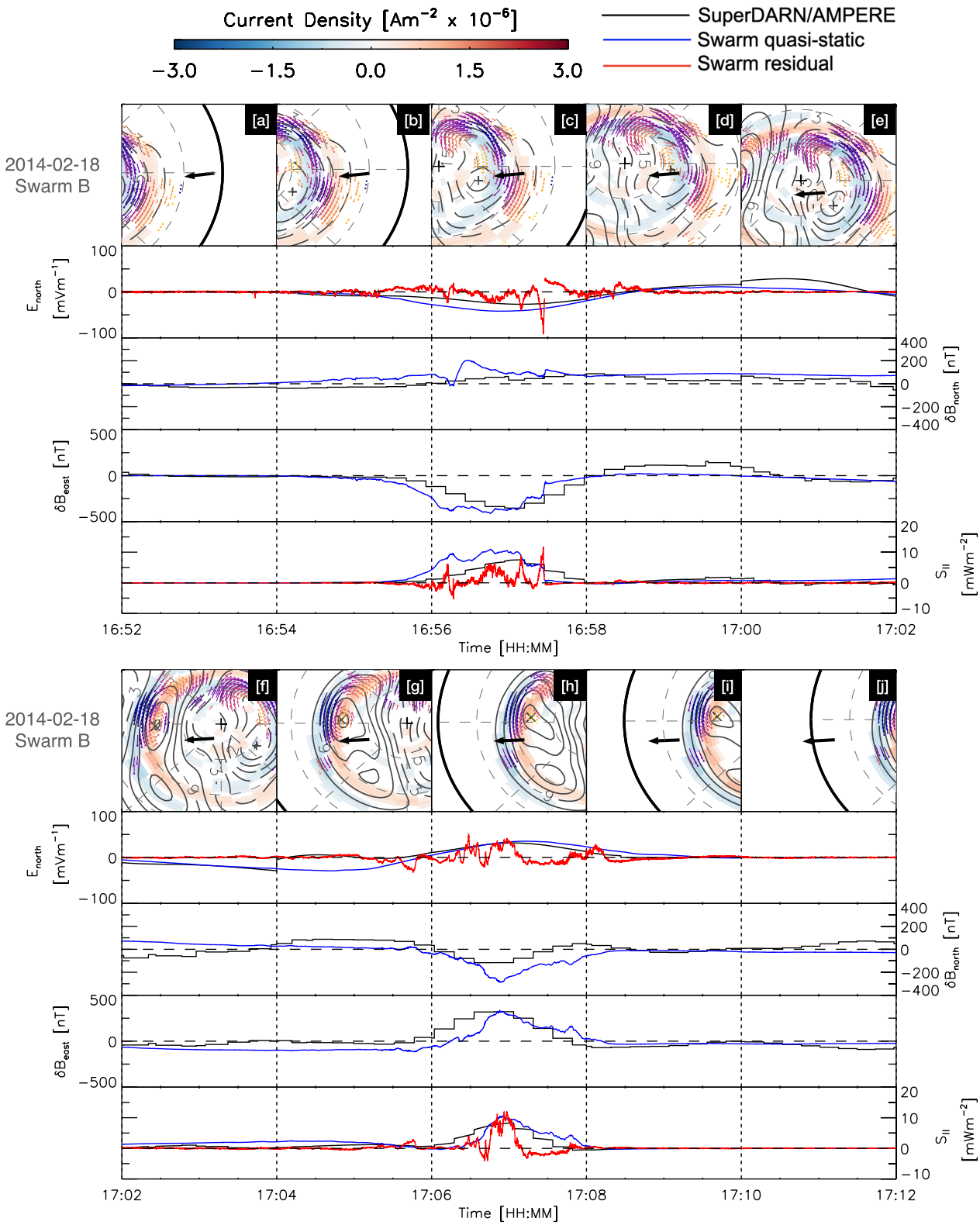

Figure 2. Swarm B-SuperDARN-AMPERE comparisons on 18 February 2018 between 16:52 and 17:12 UT. The top panels show SuperDARN electric potential contours and AMPERE field-aligned current current densities, segmented into 2-min intervals, with the Swarm trajectory in each overplotted with a black arrow. As in Figure 1a, colored velocity vectors show the location of binned SuperDARN radar data. Timeseries compare electric and magnetic fields, and Poynting fluxes. The color of the timeseries lines indicates if the data was from SuperDARN or AMPERE (black), Swarm quasi-static (blue), and Swarm residual (red).

Swarm measurements, as more data tends to lessen the impact of the empirical model. Overall, this event illustrates that our filtering scheme for Swarm data into a quasi-static component produces a remarkable consistency with SuperDARN convection map data, when radar coverage is good. There does appear to be an underestimation of the electric field magnitude by SuperDARN in panel (c), which has been noted in previous studies (e.g., Koustov et al., 2019).

The Swarm residual electric field is close to zero except when the satellite comes into contact with the FAC regions seen by AMPERE (Figure 2, panels c and h). In contrast to $\mathbf{E}_{\mathbf{static}}$, $\delta\mathbf{E}$ contains a significant amount of structure and variability, both on small and mesoscales. Because of the good agreement between $\mathbf{E}_{\mathbf{static}}$ and SuperDARN, the spatiotemporal variability in $\delta\mathbf{E}$ essentially corresponds to that which is underestimated by the SuperDARN convection map.

For the Swarm $\delta\mathbf{B}$ comparisons with AMPERE, there is an excellent correspondence in the eastward direction with clearly defined FAC signatures (i.e., a westward $\delta\mathbf{B}$ deflection on the dawnside and an eastward one on the duskside). We do note however that Swarm appears to see the FACs slightly earlier in the eastward $\delta\mathbf{B}$ than AMPERE on the dawnside (panels b and c), and later on the duskside (panel h). This implies that in this case the AMPERE fit is placing the FACs slightly poleward of Swarm observations. For northward $\delta\mathbf{B}$, there is a poorer correspondence between Swarm and AMPERE which is slightly more consistent on the duskside compared to dawn. In Figure 2c, for example, the northward $\delta\mathbf{B}$ from Swarm B shows variable structures whilst AMPERE shows a smooth transition between the R1 and R2 dawnside FACs. In panel (h), for the duskside FAC region, the northward $\delta\mathbf{B}$ differences between Swarm and AMPERE appear mostly offset in magnitude. These discontinuities between Swarm and AMPERE could be the result of the AMPERE fit being unable to resolve sub-quasi-static structures, as well as systematically underestimating $\delta\mathbf{B}$ in the north-south direction.

The bottom timeseries in Figure 2 compares the Poynting flux from Swarm with that from the SuperDARN/AMPERE method. Because $\mathbf{E}_{\mathbf{static}}$ from Swarm is well represented by the convection electric field from SuperDARN, the quasi-static Poynting flux from Swarm and SuperDARN/AMPERE correlate well. There is however a considerable amount of Poynting flux observed by Swarm that is not captured by SuperDARN/AMPERE. Indeed, the magnitude of $\mathbf{S}_{\mathrm{residual}}$ is comparable to $\mathbf{S}_{\mathrm{static}}$ in the FAC regions, illustrating that as much as ∼50% of the Poynting flux energy budget is from small and mesoscales. This large discrepancy agrees with recent work by Billett, McWilliams, Pakhotin, et al. (2022), who showed that the calculated Poynting flux decreases with increasing scale size of measurements due to increasing electric field variability. It is clear that there is multi-scale variability within $\delta\mathbf{E}$ and hence $\mathbf{S}_{\mathrm{residual}}$, likely as a result of Alfvén waves at high frequencies (e.g., Miles et al., 2018; Pakhotin et al., 2018) and plasma instabilities/shears at lower (but not quasi-static) frequencies (Cousins et al., 2013; Cousins & Shepherd, 2012). $\mathbf{S}_{\mathrm{static}}$ will thus largely depend on large-scale solar wind driving conditions, whilst the $\mathbf{S}_{\mathrm{residual}}$ embedded within the quasi-static system will depend more on season and solar cycle (Matsuo & Richmond, 2008).

Figure 3 shows two events where Swarm A crossed the duskside on 6 May 2016 (panels a–e), and two days later on 8 May 2016 (panels f–j), in the same format as Figure 2. The Kp index for the 2016-05-06 event was low (2+), and for the 2016-05-08 event indicated a moderate geomagnetic storm (6−). Note that the scales are different between panels (a–e) and (f–j), particularly the Poynting flux and eastward $\delta\mathbf{B}$, which reach significantly higher magnitudes during the storm event.

For the 6 May 2016 event in Figures 3a–3e, there was excellent SuperDARN radar data coverage of the entire dusk convection cell. The Swarm $\mathbf{E}_{\mathbf{static}}$ correlates very well with the SuperDARN convection electric field, but has an overall a larger magnitude between panels (b) and (d). Similar to Figure 2, there is a fairly poor correlation between the Swarm northward $\delta\mathbf{B}$ and AMPERE, but a very good correlation in the eastward direction. Contrasting to the event shown in Figure 2, however, is small-scale variability within the magnetic field measurements whilst Swarm traverses the FACs in panels (b) and (c). This $\delta\mathbf{B}$ variability is indicative of filamentary FACs embedded within the R1 and R2 currents (Lukianova, 2020; Neubert & Christiansen, 2003), which the fitted AMPERE data effectively only sees as smoothed-out and large-scale structures.

The correlation between the Swarm quasi-static and SuperDARN/AMPERE Poynting fluxes is once again very good in Figures 3a–3e. Interestingly, Swarm sees a sustained 40 s period of negative (upward) $\mathbf{S}_{\mathrm{static}}$ in panel (b), which SuperDARN/AMPERE does see, but to a much lesser degree (∼−6 mW m^{-2} compared to ∼−0.5 mW m^{-2}). Upward Poynting flux implies thermospheric forcing of the ionosphere (such as via a neutral wind flywheel)

10.1029/2023GL103733

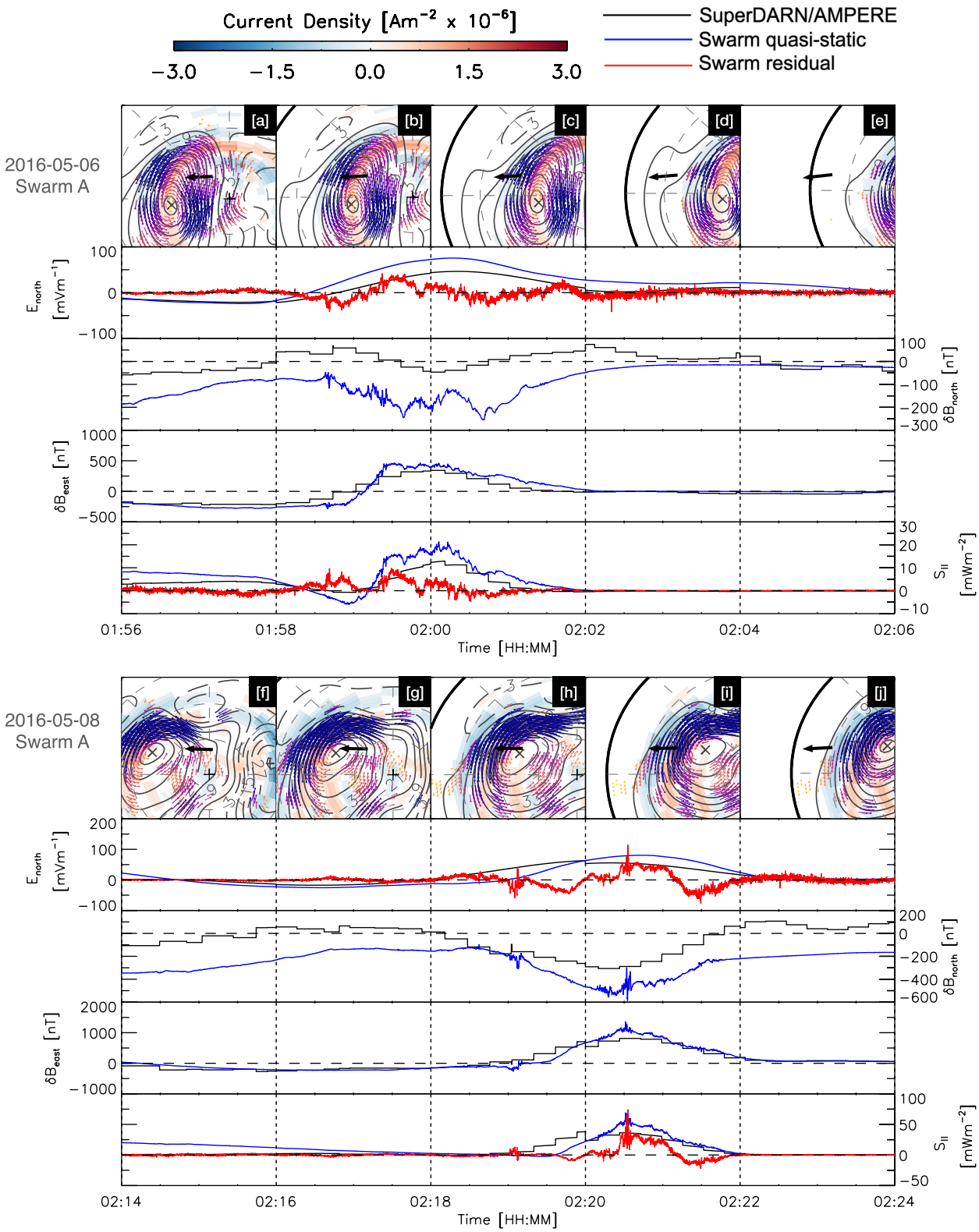

Figure 3. Same format as Figure 2, but for events on 6 May 2016 (panels a–e) and 8 May 2016 (panels f–j) with Swarm A.

rather than the other way around, leading to electromagnetic energy transferring from the atmosphere to the magnetosphere (W. Deng et al., 1993). We also note that $\mathbf{S}_{residual}$ is positive at the same time as the negative $\mathbf{S}_{static}$, and at a similar magnitude, meaning that the total Poynting flux in that 40 s period would be much closer to zero. The balance between $\mathbf{S}_{static}$ and $\mathbf{S}_{residual}$ tells us that the thermosphere can generate large-scale quasi-static electric fields whilst effectively being countered by Alfvén waves and mesoscale dynamics of magnetospheric origin, an observation that would be missed by utilizing SuperDARN and AMPERE alone.

The comparisons between Swarm, SuperDARN and AMPERE remain consistent even for storm-time events, such as that shown in Figures 3f–3j, The primary differences from a quieter event are the magnitudes of measurements, particularly the eastward $\delta\mathbf{B}$ and Poynting fluxes. Eastward $\delta\mathbf{B}$'s reach in excess of 1,000 nT for Swarm and slightly less for AMPERE, whilst both $\mathbf{S}_{static}$ and $\mathbf{S}_{residual}$ reach ∼70 mW m^{-2}. SuperDARN convection pattern and AMPERE FACs extend considerably more equatorward than the other events shown in this letter, consistent with the expanding-contracting polar cap paradigm (Cowley & Lockwood, 1992). The northward $\delta\mathbf{B}$ from AMPERE is once again significantly different from that measured by Swarm, but it does follow a similar trend, offset in magnitude.

In Figures 3f–3j, Swarm A traverses the duskside convection cell. Very small-scale wave-like fluctuations are seen in both the Swarm electric and magnetic field measurements, coincident with each other in panels (h) and (i), which propagate into $\mathbf{S}_{static}$ and $\mathbf{S}_{residual}$. The kilometer-scale sizes of these fluctuations is consistent with Alfvénic perturbations (Rother et al., 2007) occurring whilst Swarm is within the duskside FACs, similar to observations of embedded waves by Wu et al. (2020).

4. Summary

In this letter, electric and magnetic field comparisons have been made between the global scale fits of SuperDARN and AMPERE, with high spatiotemporal resolution data from the Swarm constellation. It is shown that applying a Savitsky-Golay low-pass filter of 225s to the Swarm electric field data produces a smoothed component which is exceptionally close to the electric field derived from SuperDARN convection patterns. The residual electric field from Swarm is therefore composed of fluctuations on small and mesoscales which SuperDARN is unable to capture. Effectively, we have illustrated a way of extracting the large-scale quasi-static component of the ionospheric Poynting flux from Swarm, leaving behind a residual which captures the structures embedded within.

Utilizing this new filtering scheme, three polar-pass events were examined, comparing the Swarm quasi-static ($\mathbf{S}_{static}$) and residual ($\mathbf{S}_{residual}$) Poynting fluxes to those calculated using SuperDARN and AMPERE. For all events, including a Kp 6- geomagnetic storm, the timeseries curve for $\mathbf{S}_{static}$ was very close in shape and magnitude to that derived from SuperDARN and AMPERE. $\mathbf{S}_{residual}$, however, showed a significant amount of variability and often reached or exceeded $\mathbf{S}_{static}$. In the events examined alone, small and mesoscale Poynting flux generators accounted for as much as half of the total magnetosphere-ionosphere electrodynamic energy budget. Thus, it is expected that instruments specialized in observing large-scale ionospheric structures critically underestimate the variability and magnitude of the sub-quasi-static system.

In particular, the data comparisons in this letter reveal striking structure embedded within and between the large-scale R1 and R2 FACs, indicative of mesoscale dynamics and Alfvén waves impinging on the ionosphere. These comparisons would have not been possible were it not for SuperDARN and AMPERE providing global-scale coverage of the high-latitude convection and FAC patterns, essentially forming a comprehensive map so that the Swarm data could be interpreted effectively. We stress the importance of future multi-instrument comparisons such as these to help untangle multi-scale ionospheric processes.

Data Availability Statement

16 Hz TII data from the ESA Swarm A and B satellites was obtained from https://swarm-diss.eo.esa.int, in the "Advanced/Plasma_Data/16_Hz_TIII_Cross-track_Dataset/New_baseline" directory. 50 Hz high-res magnetic field measurements were obtained from the "Level1b/Latest_baselines/MAGx_HR" directory. Fitted SuperDARN data can be downloaded from Globus, instructions of which are provided here: https://superdarn.ca/data-products. Raw SuperDARN data with DOI's can be accessed via: https://www.frdr-dfdr.ca/repo/collection/superdarn. AMPERE data can be plotted and downloaded at: http://ampere.jhuapl.edu/.

Acknowledgments
This research was supported by the European Space Agency (ESA) Living Planet Fellowship programme and by the National Sciences and Engineering Research Council of Canada (NSERC). DDB was supported by ESA under the "HLPF-SSA" project and by NSERC under CREATE Grant 479771-20. KM was supported by NSERC Discovery Grant RGPIN 05472-2017. SKV and the collection and processing of data for AMPERE was supported by the US National Science Foundation under AGS Grant 2002574. Thermal Ion Imager (TII) data processing and calibration are supported at the University of Calgary via Canadian Space Agency Grant 15SUSWARM. The authors also acknowledge the use of data from SuperDARN, an international project made possible by the national funding agencies of Australia, Canada, China, France, Italy, Japan, South Africa, Norway, the United Kingdom and the United States of America. We also thank the AMPERE team and the AMPERE Science Center for providing the Iridium derived data products.

References

Alken, P., Thébault, E., Beggan, C. D., Amit, H., Aubert, J., Baerenzung, J., et al. (2021). International geomagnetic reference field: The thirteenth generation. *Earth Planets and Space*, *73*(1), 1–25. https://doi.org/10.1186/s40623-020-01288-x

Anderson, B. J., Angappan, R., Barik, A., Vines, S. K., Stanley, S., Bernasconi, P. N., et al. (2021). Iridium communications satellite constellation data for study of Earth's magnetic field. *Geochemistry, Geophysics, Geosystems*, *22*(8), e2020GC009515. https://doi.org/10.1029/2020gc009515

Anderson, B. J., Korth, H., Waters, C. L., Green, D. L., Merkin, V. G., Barnes, R. J., & Dyrud, L. P. (2014). Development of large-scale Birkeland currents determined from the active magnetosphere and planetary electrodynamics response experiment. *Geophysical Research Letters*, *41*(9), 3017–3025. https://doi.org/10.1002/2014gl059941

Billett, D. D., McWilliams, K. A., Kerr, R. B., Makela, J. J., Chartier, A. T., Ruohoniemi, J. M., et al. (2022). Mid-latitude neutral wind responses to sub-auroral polarization streams. *Annales Geophysicae*, *40*(5), 571–583. https://doi.org/10.5194/angeo-40-571-2022

Billett, D. D., Hosokawa, K., Grocott, A., Wild, J. A., Aruliah, A. L., Ogawa, Y., et al. (2020). Multi-instrument observations of ion-neutral coupling in the dayside cusp. *Geophysical Research Letters*, *47*(4), e2019GL085590. https://doi.org/10.1029/2019gl085590

Billett, D. D., McWilliams, K. A., Pakhotin, I. P., Burchill, J. K., Knudsen, D. J., & Martin, C. J. (2022). High-resolution poynting flux statistics from the Swarm mission: How much is being underestimated at larger scales? *Journal of Geophysical Research: Space Physics*, *127*(7), e2022JA030573. https://doi.org/10.1029/2022ja030573

Billett, D. D., McWilliams, K. A., Perry, G. W., Clausen, L. B. N., & Anderson, B. J. (2022). Ionospheric energy input in response to changes in solar wind driving: Statistics from the SuperDARN and AMPERE campaigns. *Journal of Geophysical Research: Space Physics*, *127*(3), e2021JA030102. https://doi.org/10.1029/2021ja030102

Billett, D. D., Perry, G. W., Clausen, L. B. N., Archer, W. E., McWilliams, K. A., Haaland, S., et al. (2021). The relationship between large scale thermospheric density enhancements and the spatial distribution of Poynting flux. *Journal of Geophysical Research: Space Physics*, *126*(5), e2021JA029205. https://doi.org/10.1029/2021ja029205

Burchill, J. K., & Knudsen, D. J. (2016). EFI TII cross-track flow data release notes.

Burchill, J. K., & Knudsen, D. J. (2022). Swarm thermal ion imager measurement performance. *Earth Planets and Space*, *74*(1), 1–39. https://doi.org/10.1186/s40623-022-01736-w

Chulliat, A., Brown, W., Alken, P., Beggan, C., Nair, M., Cox, G., et al. (2020). The US/UK world magnetic model for 2020–2025: Technical report.

Clausen, L. B. N., Baker, J., Ruohoniemi, J. M., Milan, S. E., Coxon, J. C., Wing, S., et al. (2013). Temporal and spatial dynamics of the regions 1 and 2 Birkeland currents during substorms. *Journal of Geophysical Research: Space Physics*, *118*(6), 3007–3016. https://doi.org/10.1002/jgra.50288

Clausen, L. B. N., Baker, J. B. H., Ruohoniemi, J. M., Greenwald, R. A., Thomas, E. G., Shepherd, S. G., et al. (2012). Large-scale observations of a subauroral polarization stream by midlatitude SuperDARN radars: Instantaneous longitudinal velocity variations. *Journal of Geophysical Research*, *117*(A5), A05306. https://doi.org/10.1029/2011ja017232

Codrescu, M. V., Fuller-Rowell, T. J., & Foster, J. C. (1995). On the importance of E-field variability for Joule heating in the high-latitude thermosphere. *Geophysical Research Letters*, *22*(17), 2393–2396. https://doi.org/10.1029/95gl01909

Cousins, E. D. P., Matsuo, T., & Richmond, A. D. (2013). Mesoscale and large-scale variability in high-latitude ionospheric convection: Dominant modes and spatial/temporal coherence. *Journal of Geophysical Research: Space Physics*, *118*(12), 7895–7904. https://doi.org/10.1002/2013ja019319

Cousins, E. D. P., & Shepherd, S. G. (2012). Statistical characteristics of small-scale spatial and temporal electric field variability in the high-latitude ionosphere. *Journal of Geophysical Research*, *117*(A3), A03317. https://doi.org/10.1029/2011ja017383

Cowley, S. W. H., & Lockwood, M. (1992). Excitation and decay of solar wind-driven flows in the magnetosphere-ionosphere system. *Annales Geophysicae*, *10*, 103–115.

Deng, W., Killeen, T. L., Burns, A. G., Roble, R. G., Slavin, J. A., & Wharton, L. E. (1993). The effects of neutral inertia on ionospheric currents in the high-latitude thermosphere following a geomagnetic storm. *Journal of Geophysical Research*, *98*(A5), 7775–7790. https://doi.org/10.1029/92ja02268

Deng, Y., & Ridley, A. J. (2007). Possible reasons for underestimating Joule heating in global models: E field variability, spatial resolution, and vertical velocity. *Journal of Geophysical Research*, *112*(A9), A09308. https://doi.org/10.1029/2006ja012006

Dungey, J. W. (1961). Interplanetary magnetic field and the auroral zones. *Physical Review Letters*, *6*(2), 47–48. https://doi.org/10.1103/physrevlett.6.47

Fiori, R. A. D., Koustov, A. V., Boteler, D. H., Knudsen, D. J., & Burchill, J. K. (2016). Calibration and assessment of Swarm ion drift measurements using a comparison with a statistical convection model. *Earth Planets and Space*, *68*(1), 1–17. https://doi.org/10.1186/s40623-016-0472-7

Fogg, A. R., Lester, M., Yeoman, T. K., Burrell, A. G., Imber, S. M., Milan, S. E., et al. (2020). An improved estimation of SuperDARN Heppner-Maynard boundaries using AMPERE data. *Journal of Geophysical Research: Space Physics*, *125*(5), e2019JA027218. https://doi.org/10.1029/2019ja027218

Greenwald, R. A., Baker, K. B., Dudeney, J. R., Pinnock, M., Jones, T. B., Thomas, E. C., et al. (1995). DARN/SuperDARN: A global view of the dynamics of high-latitude convection. *Space Science Reviews*, *71*(1–4), 761–796. https://doi.org/10.1007/bf00751350

Grocott, A., Wild, J. A., Milan, S. E., & Yeoman, T. K. (2009). Superposed epoch analysis of the ionospheric convection evolution during substorms: Onset latitude dependence. *Annales Geophysicae*, *27*(2), 591–600. https://doi.org/10.5194/angeo-27-591-2009

Heppner, J. P., & Maynard, N. C. (1987). Empirical high-latitude electric field models. *Journal of Geophysical Research*, *92*(A5), 4467–4489. https://doi.org/10.1029/ja092ia05p04467

Iijima, T., & Potemra, T. A. (1976). Field-aligned currents in the dayside cusp observed by Triad. *Journal of Geophysical Research*, *81*(34), 5971–5979. https://doi.org/10.1029/ja081i034p05971

Ivarsen, M. F., Park, J., Kwak, Y.-S., Jin, Y., Knudsen, D. J., & Clausen, L. B. N. (2020). Observational evidence for the role of Hall conductance in Alfvén wave reflection. *Journal of Geophysical Research: Space Physics*, *125*(12), e2020JA028119. https://doi.org/10.1029/2020ja028119

Keiling, A., Thaller, S., Wygant, J., & Dombeck, J. (2019). Assessing the global Alfvén wave power flow into and out of the auroral acceleration region during geomagnetic storms. *Science Advances*, *5*(6), eaav8411. https://doi.org/10.1126/sciadv.aav8411

Knipp, D. J., Matsuo, T., Kilcommons, L., Richmond, A., Anderson, B., Korth, H., et al. (2014). Comparison of magnetic perturbation data from LEO satellite constellations: Statistics of DMSP and AMPERE. *Space Weather*, *12*(1), 2–23. https://doi.org/10.1002/2013sw000987

Knudsen, D. J., Burchill, J. K., Buchert, S. C., Eriksson, A. I., Gill, R., Wahlund, J.-E., et al. (2017). Thermal ion imagers and Langmuir probes in the Swarm electric field instruments. *Journal of Geophysical Research: Space Physics*, *122*(2), 2655–2673. https://doi.org/10.1002/2016ja022571

Koustov, A. V., Lavoie, D. B., Kouznetsov, A. F., Burchill, J. K., Knudsen, D., & Fiori, R. A. D. (2019). A comparison of cross-track ion drift measured by the Swarm satellites and plasma convection velocity measured by SuperDARN. *Journal of Geophysical Research: Space Physics*, *124*(6), 4710–4724. https://doi.org/10.1029/2018ja026245

Leger, J.-M., Bertrand, F., Jager, T., Le Prado, M., Fratter, I., & Lalaurie, J.-C. (2009). Swarm absolute scalar and vector magnetometer based on helium 4 optical pumping. *Procedia Chemistry*, *1*(1), 634–637. https://doi.org/10.1016/j.proche.2009.07.158

Lomidze, L., Burchill, J. K., Knudsen, D. J., Kouznetsov, A., & Weimer, D. R. (2019). Validity study of the Swarm horizontal cross-track ion drift velocities in the high-latitude ionosphere. *Earth and Space Science*, *6*(3), 411–432. https://doi.org/10.1029/2018ea000546

Lühr, H., Park, J., Gjerloev, J. W., Rauberg, J., Michaelis, I., Merayo, J. M. G., & Brauer, P. (2015). Field-aligned currents' scale analysis performed with the Swarm constellation. *Geophysical Research Letters*, *42*(1), 1–8. https://doi.org/10.1002/2014gl062453

Lukianova, R. (2020). Swarm field-aligned currents during a severe magnetic¡? xmltex\break?¿ storm of September 2017. *Annales Geophysicae*, *38*(1), 191–206. https://doi.org/10.5194/angeo-38-191-2020

Matsuo, T., & Richmond, A. D. (2008). Effects of high-latitude ionospheric electric field variability on global thermospheric Joule heating and mechanical energy transfer rate. *Journal of Geophysical Research*, *113*(A7), A07309. https://doi.org/10.1029/2007ja012993

Miles, D. M., Mann, I. R., Pakhotin, I. P., Burchill, J. K., Howarth, A. D., Knudsen, D. J., et al. (2018). Alfvénic dynamics and fine structuring of discrete auroral arcs: Swarm and e-POP observations. *Geophysical Research Letters*, *45*(2), 545–555. https://doi.org/10.1002/2017gl076051

Neubert, T., & Christiansen, F. (2003). Small-scale, field-aligned currents at the top-side ionosphere. *Geophysical Research Letters*, *30*(19), 2010. https://doi.org/10.1029/2003gl017808

Pakhotin, I. P., Mann, I. R., Lysak, R. L., Knudsen, D. J., Gjerloev, J. W., Rae, I. J., et al. (2018). Diagnosing the role of Alfvén waves in magnetosphere-ionosphere coupling: Swarm observations of large amplitude nonstationary magnetic perturbations during an interval of northward IMF. *Journal of Geophysical Research: Space Physics*, *123*(1), 326–340. https://doi.org/10.1002/2017ja024713

Rother, M., Schlegel, K., & Lühr, H. (2007). CHAMP observation of intense kilometer-scale field-aligned currents, evidence for an ionospheric Alfvén resonator. *Annales Geophysicae*, *25*(7), 1603–1615. https://doi.org/10.5194/angeo-25-1603-2007

Ruohoniemi, J. M., & Baker, K. B. (1998). Large-scale imaging of high-latitude convection with super dual auroral radar network HF radar observations. *Journal of Geophysical Research*, *103*(A9), 20797–20811. https://doi.org/10.1029/98ja01288

Ruohoniemi, J. M., & Greenwald, R. A. (1996). Statistical patterns of high-latitude convection obtained from Goose Bay HF radar observations. *Journal of Geophysical Research*, *101*(A10), 21743–21763. https://doi.org/10.1029/96ja01584

Senior, C., Cerisier, J.-C., Rich, F., Lester, M., & Parks, G. K. (2002). Strong sunward propagating flow bursts in the night sector during quiet solar wind conditions: SuperDARN and satellite observations. *Annales Geophysicae*, *20*(6), 771–779. https://doi.org/10.5194/angeo-20-771-2002

Shepherd, S. G. (2014). Altitude-adjusted corrected geomagnetic coordinates: Definition and functional approximations. *Journal of Geophysical Research: Space Physics*, *119*(9), 7501–7521. https://doi.org/10.1002/2014ja020264

Sofko, G. J., Greenwald, R., & Bristow, W. (1995). Direct determination of large-scale magnetospheric field-aligned currents with SuperDARN. *Geophysical Research Letters*, *22*(15), 2041–2044. https://doi.org/10.1029/95gl01317

Thomas, E. G., & Shepherd, S. G. (2018). Statistical patterns of ionospheric convection derived from mid-latitude, high-latitude, and polar SuperDARN HF radar observations. *Journal of Geophysical Research: Space Physics*, *123*(4), 3196–3216. https://doi.org/10.1002/2018ja025280

Walach, M.-T., Grocott, A., Staples, F., & Thomas, E. G. (2022). Super dual auroral radar network expansion and its influence on the derived ionospheric convection pattern. *Journal of Geophysical Research: Space Physics*, *127*(2), e2021JA029559. https://doi.org/10.1029/2021ja029559

Waters, C. L., Anderson, B. J., Green, D. L., Korth, H., Barnes, R. J., & Vanhamäki, H. (2020). Science data products for AMPERE. Ionospheric multi-spacecraft analysis tools: Approaches for deriving ionospheric parameters (pp. 141–165).

Waters, C. L., Anderson, B. J., Greenwald, R. A., Barnes, R. J., & Ruohoniemi, J. M. (2004). High-latitude poynting flux from combined Iridium and SuperDARN data. *Annales Geophysicae*, *22*(8), 2861–2875. https://doi.org/10.5194/angeo-22-2861-2004

Waters, C. L., Anderson, B. J., & Liou, K. (2001). Estimation of global field aligned currents using the Iridium® system magnetometer data. *Geophysical Research Letters*, *28*(11), 2165–2168. https://doi.org/10.1029/2000gl012725

Weimer, D. R. (2001). Maps of ionospheric field-aligned currents as a function of the interplanetary magnetic field derived from Dynamics Explorer 2 data. *Journal of Geophysical Research*, *106*(A7), 12889–12902. https://doi.org/10.1029/2000ja000295

Wu, J., Knudsen, D. J., Gillies, D. M., & Burchill, J. K. (2020). Swarm survey of Alfvénic fluctuations and their relation to nightside field-aligned current and auroral arc systems. *Journal of Geophysical Research: Space Physics*, *125*(3), e2019JA027220. https://doi.org/10.1029/2019ja027220

Yu, Y., Cao, J., Pu, Z., Jordanova, V. K., & Ridley, A. (2022). Meso-scale electrodynamic coupling of the Earth magnetosphere-ionosphere system. *Space Science Reviews*, *218*(8), 74. https://doi.org/10.1007/s11214-022-00940-0

Zou, S., Lyons, L. R., Wang, C.-P., Boudouridis, A., Ruohoniemi, J. M., Anderson, P. C., et al. (2009). On the coupling between the Harang reversal evolution and substorm dynamics: A synthesis of SuperDARN, DMSP, and IMAGE observations. *Journal of Geophysical Research*, *114*(A1), A01205. https://doi.org/10.1029/2008ja013449